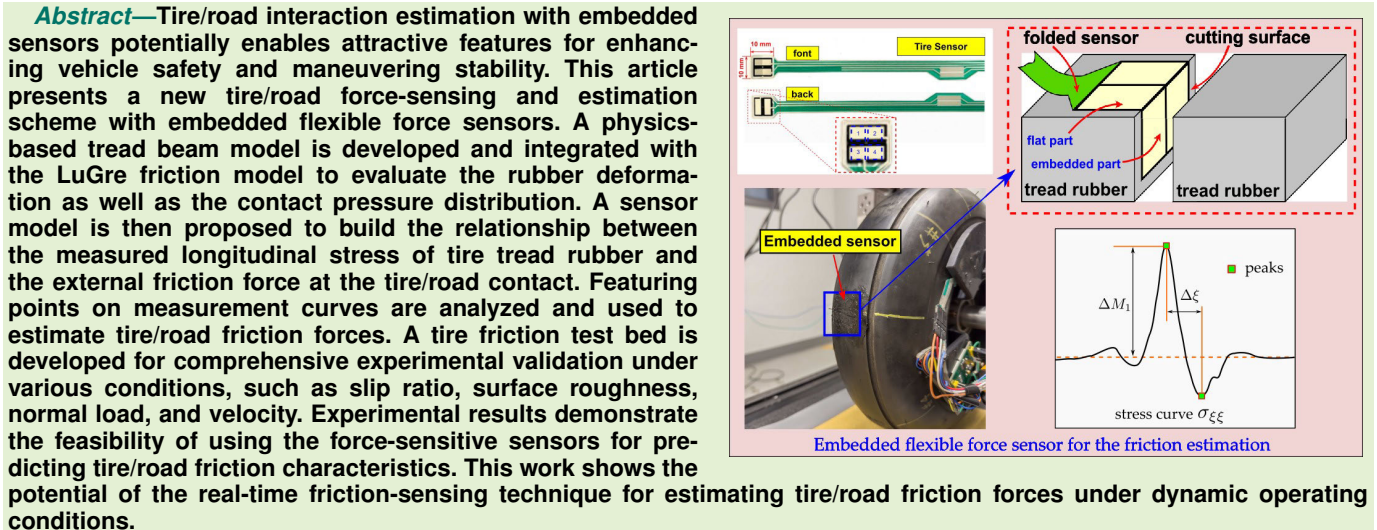


# Dynamic Tire/Road Friction Estimation With Embedded Flexible Force Sensors

Xunjie Chen<sup>ID</sup>, Hrishikesh Sathyaranarayanan<sup>ID</sup>, Yongbin Gong,  
Jingang Yi<sup>ID</sup>, Senior Member, IEEE, and Hao Wang<sup>ID</sup>



**Index Terms**—Friction prediction, tire sensor, tire test bed, tire–road interaction model.

## I. INTRODUCTION

TIRES are the only component that is in contact with the road surface and provides thrust/braking forces for ground vehicle operation. Tire/road contact characteristics significantly impact vehicle dynamics and maneuvering stability. With the help of emerging sensor technologies and “smart tire” development, tire/road contact conditions can be obtained for accurate interaction modeling and force predictions [1], [2]. Various types of embedded tire sensors, including accelerom-

eters [3], [4], [5], [6], [7], [8], acoustic sensors [9], strain gauges [10], [11], [12], [13], [14], piezoelectric sensors [15], [16], [17], [18], and force-sensing resistors [19], [20], [21], were reported. Raw sensor measurements are collected and processed to extract tire/road contact characteristics (e.g., contact load and friction force, contact length, tire velocity, and slip angle). Only local and temporal information of the contact patch is directly measured, and additional sensing models are needed to interpret the sensor measurements and estimate tire/road contact forces.

Because of the sensitivity to the vibrations excited by the texture of the contact patch, accelerometers were commonly used. Three tri-axis accelerometers were attached on the inner surface of the tire to detect friction potential indicators on different friction levels (ice and concrete) [4]. In [5], longitudinal and lateral acceleration profiles were used to obtain the contact length and lateral deflection, respectively. By fitting a tire brush model, the lateral force and align moment were estimated. In [6], accelerometers were used to predict tire forces through establishing three different machine learning schemes and training algorithms. Instead of estimating tire forces, various types of neural networks were used to develop a road surface classification tool using data collected from accelerometers embedded inside the tire [7], [8]. Meanwhile,

Hao Wang is with the Department of Civil and Environmental Engineering, Rutgers University, Piscataway, NJ 08854 USA (e-mail: hw261@soe.rutgers.edu).

Digital Object Identifier 10.1109/JSEN.2023.3313002

Manuscript received 24 June 2023; revised 21 August 2023; accepted 2 September 2023. Date of publication 12 September 2023; date of current version 31 October 2023. This work was supported in part by the Federal Aviation Administration (FAA) under Contract 692M15-21-T-00003. The associate editor coordinating the review of this article and approving it for publication was Prof. Mohsen Asadnia. (*Corresponding authors:* Jingang Yi; Hao Wang.)

Xunjie Chen, Yongbin Gong, and Jingang Yi are with the Department of Mechanical and Aerospace Engineering, Rutgers University, Piscataway, NJ 08854 USA (e-mail: xc337@rutgers.edu; yg283@scarletmail.rutgers.edu; jgyi@rutgers.edu).

Hrishikesh Sathyaranarayanan was with the Department of Mechanical and Aerospace Engineering, Rutgers University, Piscataway, NJ 08854 USA. He is now with the Department of Mechanical Engineering and Material Science, Yale University, New Haven, CT 06511 USA (e-mail: hrishi.sathyaranarayanan@yale.edu).

Jingang Yi is with the Department of Civil and Environmental Engineering, Rutgers University, Piscataway, NJ 08854 USA (e-mail: jgyi@rutgers.edu).

evaluated in [8]. However, it is challenging to remove the influence of sensing noise. Many strain-based sensors were used to estimate tire rubber deformation. Fuzzy rules were established to estimate contact variables, such as rolling radius, contact length, and tire rotation speed [12], [13]. Based on the previous studies, a new method using strain profile and support vector machines was presented to estimate the tire adhesion region and to detect tire slip in [14]. Strain gauges were equipped on large lug tires on terrains to provide longitudinal and lateral resistance force estimations [22]. An analytical flexible ring model was proposed to evaluate the strain distribution with a system identification method [23]. In [24], the flexible ring model was identified by using an array of strain gauges. The abovementioned strain-based flexible ring models in [23], [24], [25] involved a series of model parameters that need to be estimated. Other model-free methods using strain information were also reported. A polyvinylidene fluoride (PVDF) sensor was used to detect normal pressure and longitudinal strain on different surfaces [15]. In [16], a cylindrical PVDF sensor was designed to obtain the lateral deformation, and by fitting experimental deflection profile using the parabolic curve, lateral force was estimated. In [17], a mathematical model was developed to obtain the relationship between the sensor charge profile and the tire rubber deformation. A neural network model was built by feeding the PVDF measurements to predict the normal load, slip angle, and tire forces [18]. A data-driven-based tire capacity identification framework and a UniTire model were used for friction coefficient estimation [26].

Different from strain-based sensors, the pressure-sensitive, electric conductive rubber-based sensors can directly measure forces/stresses of the rubber on the contact patch [19], [21]. Fully printed and flexible carbon nanotube transistors were used to map the tire pressure and the tread depth differentials [27]. A sensor interpretation model was developed by using the beam-spring model, and the results confirmed the feasibility for predicting the static tire/road interaction [20]. The extended work in [28] combined the LuGre friction model and the beam-spring model to capture stick/slip interactions, and the work in [29] further considered hydrodynamics effects. However, force-sensitive sensors in [19], [20], [21], and [28] were only applied to predict forces in stationary conditions. The internal stress (force) under dynamic rolling situation is significantly different with the stationary case. Aforementioned studies focused on either the estimation of the contact features (e.g., contact pressure distribution and vertical load) or using data-driven methods (e.g., fuzzy, machine learning). No further analytical relationship between the strain and the friction force was studied to show how local measurements vary when external forces change.

In this article, we present a new force-sensing and estimation scheme for dynamic tire/road interactions by using embedded force sensors that directly capture stress information. A physics-based tread beam model and the LuGre friction model are integrated to describe the internal stress related to rubber deformation in the vertical and longitudinal directions. Then, a sensor interpretation model is discussed to extract the longitudinal stress that is captured by direct sensor measurements. Comprehensive experiments on the tire friction test platform are conducted to validate the sensor sensitivity

to tire operating conditions, such as relative slip, vertical load, and tire velocity. Experimental results demonstrate the promising application of the sensor for predicting tire/road interactions. The main contribution of this work lies in the real-time tire/road friction force and the dynamic interaction estimation using the embedded piezoresistant flexible sensors. The most closest research work focuses on strain-based sensors, and few investigate tire internal stress in dynamic rotation applications with embedded sensors. In [21], the friction force was given as a known boundary condition to compute internal forces on the contact patch under stationary conditions. It is difficult to apply this stress computation method on rotation scenarios. Furthermore, no explicit relation was established in [21] between the sensor measurement and friction forces under tire rotation conditions.

The rest of this article is organized as follows. We introduce the embedded sensor and the overview of the modeling approaches in Section II. Section III presents a tire/road interaction stress model. A sensor interpretation model is analyzed in Section IV. Experiments and results are discussed in Section V. Finally, we summarize the concluding remarks in Section VI.

## II. EMBEDDED FLEXIBLE TIRE SENSOR AND MODELING FRAMEWORK

**Fig. 1(a)** shows the force-sensitive-based sensor (RX-M0202S from RouXi Electronic Technology Company Ltd.). The sensor is small and square shaped ( $10 \times 10$  mm for the total sensing area) with four distributed sensing cells. By choosing an appropriate connection circuit, each sensing cell generates independent output signal that is proportional to the force perpendicularly applied on the sensing area. As shown in **Fig. 1(b)**, the tire tread was cut transversely and perpendicularly along the center line of the tire (cyan line). The sensor film was first folded, dividing two rows of sensing units, and embedded inside the tire tread rubber layer. The first row was attached and glued on the internal surface of the tire tread, which directly contacted the tire inner tube and captured the normal load. The embedded row was inserted into the tread, and this allowed to measure the inner force of the tread. To maintain good and homogeneous contact property with rubber, a filling and gluing process was carefully operated. A soft silicone material was chosen to fill the cutting crack after inflating the inner tube. High-performance rubber glue was used to seal the silicone at the cutting surface area and also to allow the silicone filler flexibility to make the sensor reading consistent. By observing and comparing the experimental results, the embedding method confirmed negligible destructive effect on the tire tread internal stress.

**Fig. 2** illustrates the overview approaches to obtain the real-time tire/road interaction forces and frictional characteristic. We first develop an integrated tire tread beam and the LuGre friction model to provide normal pressure distribution and reveal the internal longitudinal stress distribution. The feature points of the tire internal stress distribution are used to represent the magnitude of the external friction force and the elongation of the tire rubber layer on the contact patch. A sensor interpretation model is then developed to build and bridge the connection of the sensor measurements and

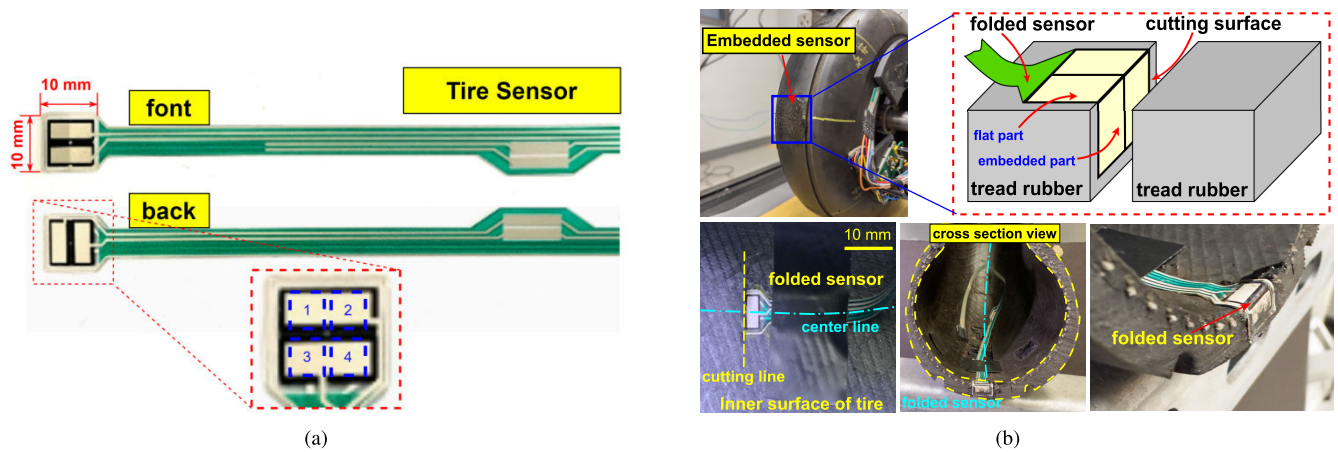


**Fig. 1.** (a) Embedded flexible tire force sensor. Top: front side view. Bottom: back side view. (b) Folded sensor is embedded inside the tire tread layer and general schematic of the embedded sensor in the tire tread rubber.

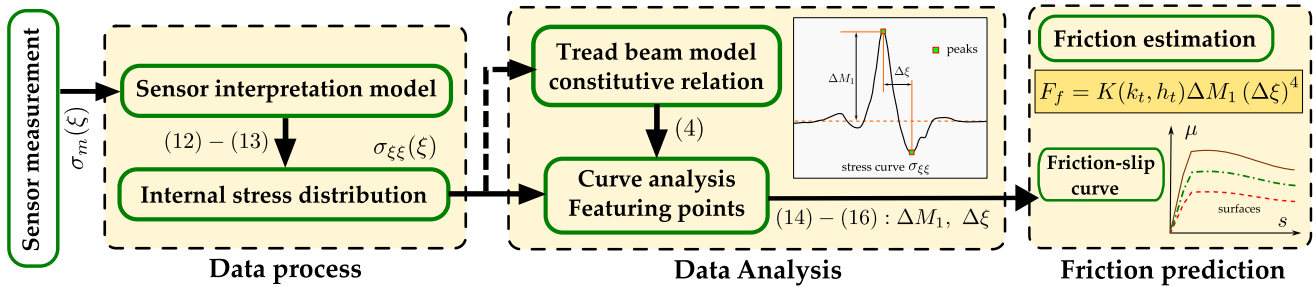


**Fig. 2.** Overall pipeline to illustrate the various modeling modules and sensor data processing and prediction methods.

the internal longitudinal stress distribution. The outcomes provide the real-time friction force prediction as well as the tire/road friction coefficient–slip characteristic on different contact surfaces, which plays a critical role for vehicle dynamics and operations. In Sections III and IV, we present the tire internal stress model and the sensor interpretation model, respectively.

### III. TIRE/ROAD INTERACTION STRESS MODELS

#### A. Tire/Road Interaction Deformation

Fig. 3(a) shows the modeling schematic of the tire/road interaction. The tire motion is considered only in the longitudinal direction. The vertical and longitudinal deformations and forces of the tire/road contact patch are of interest. The tire is running and rotating on the firm road surface with the longitudinal translation velocity  $v_x$  and angular velocity  $\omega$ . The total normal load, denoted by  $F_z$ , and the resultant longitudinal friction force, denoted by  $F_f$ , are considered on the contact patch. We define the tire slip ratio  $s = |v_x - \omega R_e|/\max(v_x, \omega R_e)$ , where  $R_e$  is the effective rolling radius. The effective rolling radius is defined as the ratio between  $v_x$  and  $\omega$  [30]. In this article, the value of  $R_e$  can be estimated by the loaded height of the tire center; see Fig. 3(a). The road friction coefficient is defined as  $\mu = F_f/F_z$ .

Unlike the flexible ring model with the entire circumferential tread layer, only the rubber in an effective segment, shown in Fig. 3(a), is deformed significantly during the contact. The arc length of the effective segment is denoted as  $l_e$ , and the length and the thickness of the tire/road contact patch are

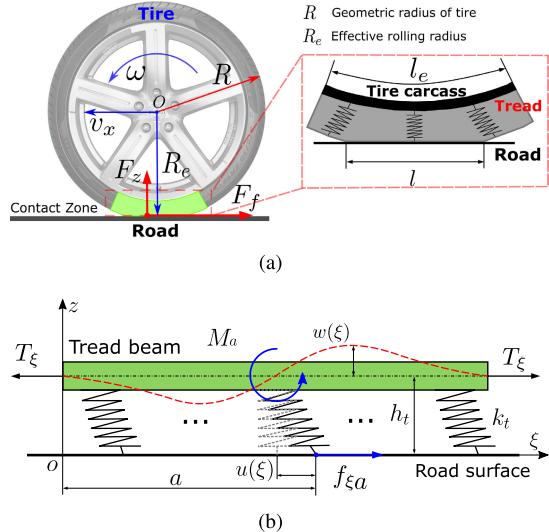


**Fig. 3.** Schematic of the tread beam model for the tire–road contact. (a) Tire–road contact problem is considered as a beam model on elastic foundation. (b) Tread beam model captures the vertical deformation given an external moment,  $M_a$ .

denoted as  $l$  and  $h_t$ , respectively. The tire carcass is much stiffer than the tread rubber, and therefore, its deflection is negligible. Considering that the effective segment length  $l_e$  is much shorter than the entire circumferential length, the tire carcass is approximated as a straight beam on the elastic foundation. Fig. 3(b) illustrates the tread beam modeling configuration. Virtual springs under the beam represent the

vertical elasticity of rubber. The resultant frictional force generates longitudinal deflection at spring tips as well as a bending moment contributing to the vertical deflection. The vertical deflection results in the variation of the normal load distribution.

The local coordinate for the tread beam model is chosen as  $\xi oz$ . The origin is located at the leading edge of the effective segment, and the positive direction is from the leading to the trailing edges. The positive direction of the  $z$ -axis is upward. We denote  $w(\xi)$  and  $u(\xi, z)$  as the vertical and longitudinal deformations at position  $\xi \in [0, l_e]$  and  $z \in [0, h_t]$ , respectively. We now compute  $w(\xi)$ ,  $u(\xi, z)$ , and the internal stress.

By the beam theory, the vertical deformation  $w(\xi)$  is uniformed across the thickness and governed by [31]

$$EI \frac{d^4 w(\xi)}{d\xi^4} - T_\xi \frac{d^2 w(\xi)}{d\xi^2} + k_t w(\xi) = 0$$

where  $T_\xi$  is the internal force in the longitudinal direction,  $E$  and  $I$  are, respectively, the equivalent elastic modulus and area moment of inertia of the tread beam, and  $k_t$  is the vertical stiffness of the tread rubber. The resultant bending moment  $M(\xi)$  is obtained by

$$M(\xi) = -EI \frac{d^2 w(\xi)}{d\xi^2}.$$

Given an external moment  $M_a$  applied at  $\xi = a$ , the vertical deformation  $w(\xi)$  under  $M_a$  is expressed as follows:

$$w(\xi) = \frac{M_a}{2\beta_1\beta_2 EI} e^{-\beta_1|\xi-a|} \sin \beta_2(\xi-a) \quad (1)$$

where coefficients  $\beta_1$  and  $\beta_2$  are given by

$$\beta_1, \beta_2 = \sqrt{\frac{k_t}{4EI}} \sqrt{1 \pm \frac{T_\xi}{\sqrt{4EI}k_t}}. \quad (2)$$

The corresponding normal load variation, denoted by  $\Delta p_z(\xi)$ , is proportional to the vertical deflection, namely,

$$\Delta p_z(\xi) = -k_t w(\xi).$$

The negative sign in the above equation is taken to consider that springs at the location with  $w(\xi) < 0$  are compressed and further increase the normal load. The tire/road normal pressure at  $\xi$ , denoted by  $p_{z0}(\xi)$ , is considered as a soft intruder contacting with a rigid object and is expressed as follows [32]:

$$p_{z0}(\xi) = \frac{E^*}{\pi R_b} \int_{\max(r, \frac{l}{2})}^{l_e/2} \frac{2\sqrt{4x^2 - l^2} - l \cos^{-1}\left(\frac{l}{2x}\right)}{2\sqrt{x^2 - r^2}} dx$$

where  $r = \xi - l_e/2$ ,  $E^*$  is the effective elasticity modulus, and  $R_b$  is the radius at the bending shoulder of the tire after loading. The total normal pressure distribution is then given as follows:

$$p_z(\xi) = p_{z0}(\xi) + \Delta p_z(\xi). \quad (3)$$

## B. Internal Stress Model

We describe the constitutive relation between the internal stress in the longitudinal direction, denoted by  $\sigma_{\xi\xi}$ , and the strain (deformation) as follows [31]:

$$\sigma_{\xi\xi}(\xi, z) = \frac{E}{1-\nu^2} [\epsilon_\xi(\xi, z) + \nu \epsilon_z(\xi)] \quad (4)$$

where  $\nu$  is the Poisson ratio of the tread rubber.  $\epsilon_\xi(\xi, z)$  and  $\epsilon_z(\xi)$  represent the strains along the longitudinal and vertical directions at  $(\xi, z)$ , respectively. The vertical deformation is assumed to be uniform across the rubber layer with the characteristic vertical length. According to the beam theory, the strains are expressed as follows:

$$\epsilon_z(\xi) = \frac{w(\xi)}{R_e}, \quad \epsilon_\xi(\xi, z) = \frac{\partial u(\xi, z)}{\partial \xi} - z \frac{\partial^2 w(\xi)}{\partial \xi^2}. \quad (5)$$

To obtain the longitudinal deformation  $u(\xi, z)$ , we first use the LuGre friction model to calculate the longitudinal deformation at the contact surface  $z = h_t$ , that is,  $u_z(\xi) := u(\xi, h_t)$ . Considering the steady state of the LuGre model and normal load dependency [33], [34], the deformation is governed by

$$\frac{du_z(\xi)}{d\xi} = sp_z(\xi) - \frac{sk_\xi}{g(v_r)} u_z(\xi). \quad (6)$$

In (6),  $k_\xi$  is the longitudinal stiffness, and the dynamic friction coefficient function is  $g(v_r) = \mu_c + (\mu_s - \mu_c)e^{-|v_r/v_s|^{1/2}}$ , where  $v_s$  is the Stribeck velocity, and  $\mu_c$  and  $\mu_s$  are Coulomb and static friction coefficients, respectively. Assuming a parabolic normal load distribution and solving (6), we obtain

$$u_z(\xi) = \frac{6g(v_r)}{k_\xi} \left[ -\left(\frac{\xi}{l_e}\right)^2 + \frac{\xi}{l_e} + U(\xi) \right]$$

where function  $U(\xi)$  is given by

$$U(\xi) = \frac{2\xi}{x_a l_e} - \frac{1}{x_a} \left( 1 + \frac{2}{x_a} \right) (1 - e^{x_a \xi / l_e}), \quad x_a = \frac{sk_\xi l_e}{g(v_r)}.$$

The contact patch can be partitioned into an adhesion and a sliding regions. By the results in [33], the deformation by (6) only holds for the adhesion region of the contact patch, while the deformation in the sliding region is given by

$$u_z(\xi) = g(v_r) p_z(\xi) / k_\xi.$$

Therefore, the deformation by the external friction force is given by [33]

$$u_z(\xi) = \begin{cases} \frac{6g(v_r)}{k_\xi} \left[ -\left(\frac{\xi}{l_e}\right)^2 + \frac{\xi}{l_e} + U(\xi) \right], & \text{adhesion} \\ g(v_r) p_z(\xi) / k_\xi, & \text{sliding.} \end{cases} \quad (7)$$

The steady-state calculation above does not incorporate the tire relaxation effect. The temporal expression of the purely sliding deformation  $u_s$  is captured by [35]

$$\frac{du_s}{dt} = v_x - \left[ R_e \omega + R |\omega| \left( \frac{u_s}{l_e} \right) \right] \quad (8)$$

where  $R$  is the unloaded geometrical radius of the tire. We approximate  $l_e \approx R$  for simplicity and solve (8) to obtain

$$u_s(t) = \frac{sv_x}{|\omega|} (1 - e^{-|\omega|t}).$$

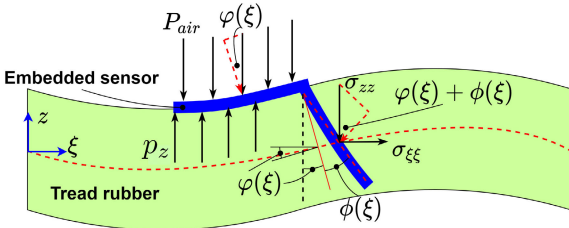


**Fig. 4.** Schematic of the embedded force sensor inside the tire tread layer. The normal stress  $\sigma_{\xi\xi}$  contributes to measurement  $\sigma_m$  from sensing units.

Considering the traveling time  $t_x = l/v_x$ , the evolution of the deformation is computed as  $u_{s0} = u_s(t_x) = (sv_x/|\omega|)(1 - e^{-|\omega|l/v_x})$ . We regulate the deformation of (7) as follows:

$$u_z(\xi) = \begin{cases} u_z(\xi) \text{ by (7),} & \text{if } u_z(\xi) \leq u_{s0} \\ u_{s0}, & \text{otherwise.} \end{cases} \quad (9)$$

The  $u_{s0}$  value increases, as the velocity  $v_x$  becomes large. There is a critical velocity beyond which the deformation related to (7) becomes dominant and eventually satisfies  $u_z(\xi) = u_{s0}$ .

The shear deformation on the contact surface is assumed as the maximum deflection of the cantilever beam. Then, by using the Euler–Bernoulli beam theory [20], the deformation along the thickness direction is obtained as follows:

$$u(\xi, z) = \frac{u_z(\xi)}{2h_t^3} \left( z^3 + \frac{3}{2}h_t z^2 - \frac{9}{4}h_t^2 z + \frac{5}{8}h_t^3 \right). \quad (10)$$

Using (1), (5), and (10), we obtain the internal stress  $\sigma_{\xi\xi}(\xi, z)$  from (4).

#### IV. SENSOR INTERPRETATION MODEL AND FRICTION ESTIMATION

##### A. Tire Sensor Interpretation Model

Fig. 4 shows the schematic of the embedded sensor in the tire tread rubber. Taking advantages of distributed sensing and flexibility, the embedded sensor measures both the vertical and longitudinal force (stress). It is assumed that pressure variation across the thickness direction is negligible due to the thin tire rubber layer. The pressure applied on the inner surface of the sensing units is denoted as  $P_s = (P_{\text{air}} - p_z) \cos \varphi(\xi)$ , where  $P_{\text{air}}$  is inflation pressure of the inner tube and  $\varphi(\xi)$  is the bending angle with respect to the longitudinal direction; see Fig. 4. Therefore, we obtain

$$\varphi(\xi) = \cos^{-1} \left( \frac{P_s}{P_{\text{air}} - p_z} \right).$$

As a result of the small longitudinal deformation at the contact surface, the tread rotation angle is

$$\phi(\xi) \approx u_z(\xi)/h_t.$$

By superposition, the total rotation angle of the embedded sensor is  $\varphi(\xi) + \phi(\xi)$ . As shown in Fig. 4, the measurement stress  $\sigma_m$  on the embedded sensing unit is computed as follows:

$$\sigma_m(\xi) = \sigma_{zz} \sin[(\varphi(\xi) + \phi(\xi))] - \sigma_{\xi\xi} \cos[(\varphi(\xi) + \phi(\xi))] \quad (11)$$

where normal stress  $\sigma_{zz}$  in the vertical direction is estimated as  $\sigma_{zz} \approx p_z$  due the thin rubber layer.

From (11), the normal stress  $\sigma_{\xi\xi}$  (evaluated at  $z = h_t/2$  so that we drop the  $\sigma_{\xi\xi}$ 's dependency on  $z$ ) is obtained as follows:

$$\sigma_{\xi\xi}(\xi) \approx \frac{p_z(\xi) \sin(\varphi(\xi) + \phi(\xi)) - \sigma_m(\xi)}{\cos(\varphi(\xi) + \phi(\xi))}. \quad (12)$$

##### B. Friction Estimation Based on Sensing Curves

From (12), the sensor measurements combine two force sources, vertical pressure  $p_z(\xi)$  and longitudinal stress  $\sigma_{\xi\xi}(\xi)$ . The rotation angle caused by the deformation is small, namely,  $\varphi(\xi) + \phi(\xi) \approx 0$ , and the embedded sensor can be considered perpendicular to the surface. Then, the longitudinal stress recovers to the sensor measurement, that is,

$$\sigma_{\xi\xi}(\xi) = -\sigma_m(\xi). \quad (13)$$

We take the advantage of this simplification to directly relate the constitutive relationship (4) to the measurements from the embedded sensor. Using feature points of the sensor measurements can reveal the magnitude of the external force and elongation of the tire tread on contact patch.

To interpret the sensor measurement, we first evaluate the three sources that contribute to the internal stress  $\sigma_{\xi\xi}(\xi)$  from (4) and (5), namely,  $\sigma_m(\xi) \propto \partial u(\xi, z)/\partial \xi$ ,  $-w(\xi)$ , and  $d^2 w(\xi)/d\xi^2$ . Fig. 5 illustrates the curves of the rubber deformation information and internal stress state calculated by (4). For the internal stress state, the maximum magnitude of the peak point, denoted by  $P_{s1}$ , and the first local minimum point, denoted by  $P_{s2}$ , are selected to reveal the information of the global friction force. The top plot of Fig. 5 illustrates three curves of sources. The maximum peak point  $P_{w1}$  and the minimum point  $P_{w2}$  of the  $d^2 w(\xi)/d\xi^2$  curve are of the interest. As shown in the Appendix, it is found that points  $P_{w1}$  and  $P_{s1}$  share the same circumferential position  $\xi$ , and the same for points  $P_{w2}$  and  $P_{s2}$ .  $I_1$  and  $I_2$  are denoted as the intersection points of  $w(\xi)$  and  $\partial u(\xi, z)/\partial \xi$  at the  $\xi$ -axis, respectively. It can be observed that the corresponding magnitudes of  $I_1$  and  $I_2$  are nearly zero compared with that of point  $P_{w1}$

$$w(\xi)|_{I_1} \approx 0, \quad \left. \frac{\partial u(\xi, z)}{\partial \xi} \right|_{I_2} \approx 0.$$

Therefore, for  $P_{s1}$ , the second derivative part contributes the most.

The stress amplitude of  $P_{s1}$  is denoted as  $\Delta M_1$ , and the magnitude of  $P_{w1}$  is denoted as  $A_{w1}$ . As discussed above and shown in the Appendix, we compute the maximum value of the second derivative of  $w(\xi)$  in (1) as follows:

$$\Delta M_1 \approx A_{w1} = \frac{(\beta_1^2 + \beta_2^2) \sin 2\alpha}{2\beta_1\beta_2 EI} M_a, \quad \tan \alpha = \frac{\beta_1}{\beta_2}. \quad (14)$$

The spacial distance between  $P_{s1}$  and  $P_{s2}$  is

$$\Delta \xi = \frac{3\pi}{4\beta_2}. \quad (15)$$

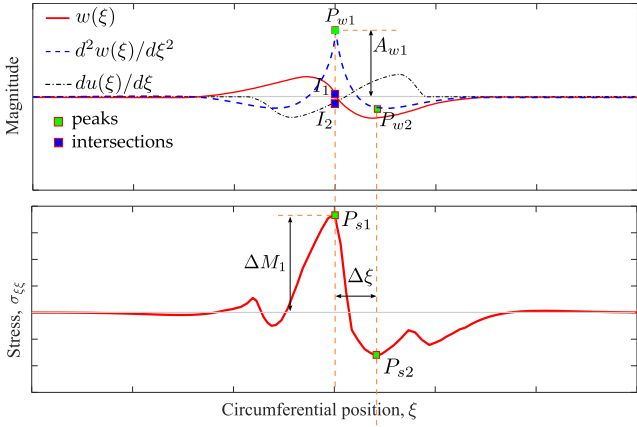


**Fig. 5.** Model predictive curves with feature points. Top: three components contributing to internal stress. Bottom: internal stress distribution.

Recall (2) that  $\beta_1 \approx \beta_2$  when the internal longitudinal force of the belt  $T_\xi$  is small compared with  $4\sqrt{EIk_t}$ . Therefore,  $\Delta M_1 \approx (M_a/EI)$ . By substituting (15) into (2), we have  $EI = (64/81)(\Delta\xi/\pi)^4 k_t$ , and plugging back into (14), we obtain

$$\Delta M_1 = \frac{M_a}{EI} = \frac{81\pi^4}{64} \frac{M_a}{(\Delta\xi)^4 k_t}.$$

Given  $F_f = M_a/h_t$ , the friction force is obtained

$$F_f = \frac{64k_t}{81\pi^4 h_t} \Delta M_1 (\Delta\xi)^4 = Kf \quad (16)$$

where  $K = (64k_t)/(81\pi^4 h_t)$  and the friction index term  $f = \Delta M_1 (\Delta\xi)^4$  reflects the external friction magnitude. The factor  $K$  would be calibrated and estimated in experiments.

From the above discussion, the right-hand side of (16) involves two direct measurements from embedded sensor, namely, the maximum magnitude  $\Delta M_1$  and the peak-to-valley distance  $\Delta\xi$  of the sensor signal  $\sigma_m(\xi)$  by (14) and (15), which is related to  $\sigma_{\xi\xi}(\xi)$  by (13). The sensor interpretation model further bridges the external friction force and local sensor measurement pattern.

## V. EXPERIMENTAL RESULTS

### A. Experimental Setup

1) *Tire Test-Bed Development:* Fig. 6(a) shows the dynamic tire friction test platform. One 11-in small aircraft tire was selected for its compact size. The outer surface was smooth, so that the testing results were not influenced by tire grooves. The tire rotation was driven by a 4-to-1 gear reduction sprocket-chain system. With the sprocket-chain and planetary gearbox (gear ratio 5:1), the motor torque was amplified significantly to overcome the tire frictional force. The tire was pressed on a modified treadmill firmly, and the treadmill was supported by a motorized jack at the center. Moving the jack upward and downward altered the tire normal load. Relative velocity and various slip conditions were maintained by controlling the translation speed of treadmill belt and tire rotation speed separately. Different friction forces were generated by creating different normal load and slip conditions.

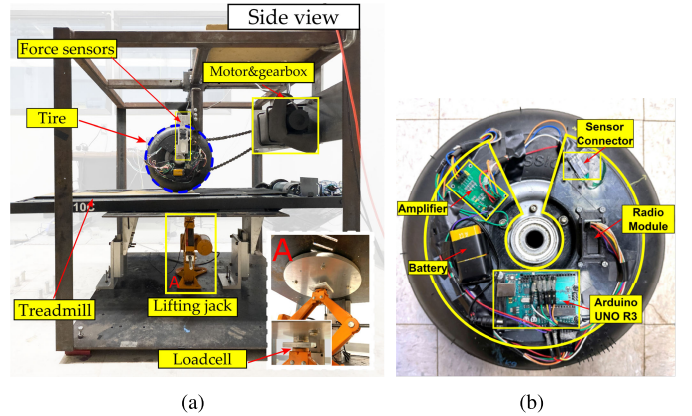


**Fig. 6.** Indoor tire friction test platform. (a) Platform includes driving torque transportation system, treadmill supporting structure, and force measurement setup. (b) Tire wireless transmission module with an embedded force sensor.

One load cell (ATI Mini45) was sandwiched and installed between the jack and treadmill to measure the tire normal load. The longitudinal friction force was measured by two bending force sensors mounted on the wheel support structure. Because of the tire rotation, all embedded sensor data need to be collected via a wireless communication. As shown in Fig. 6(b), a wireless data transmission module was designated and attached on one side of the wheel rim rotating together with the tire. The electronic unit included a sensor amplifier, a power supply, an Arduino UNO R3 board, and an extended radio module (NRF24L01 wireless transceiver). The sensor signal was first amplified and transmitted to the Arduino board. The extended radio module allowed the Arduino board to transmit data wirelessly. Simultaneously, another Arduino board was connected to a computer and functioned as a receiver. One advantage of this wireless unit was lightweight, without generating significant eccentric vibration during tire rotation. Together with the wireless transmission module, the entire sensing system (i.e., two bending force sensors, ATI Mini45 load cell, and two encoders) and the driving motor were controlled by a real-time embedded system (NI CompactRIO).

2) *Model Calibrations:* Some of the model parameters were obtained by calibrations. The rubber's elastic modulus  $E$  was measured following a standard material property testing procedure on the tension machine. For the longitudinal stiffness  $k_\xi$  in the LuGre friction model, a calibration test was conducted, and the embedded sensor was used to measure the local internal force (stress). Fig. 7(a) illustrates the calibration testing setup and a simple schematic. A simple beam model of the tread rubber was used to compute the deformation at the tip (i.e., the contact surface). According to the Euler–Bernoulli beam theory

$$\delta(h_t) = \frac{f_s(h_t)h_t^3}{3EI} \quad (17)$$

where  $\delta_t(h_t)$  and  $f_s(h_t)$ , respectively, denote the local deformation and force at the beam tip, namely, the contact surface.

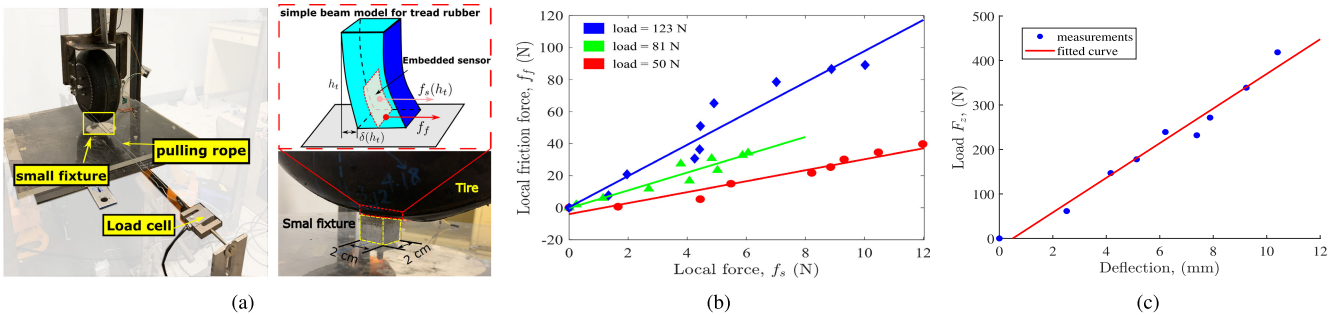


**Fig. 7.** Calibration of the longitudinal and vertical stiffness of the tire tread. (a) Setup of the static pulling test for the longitudinal stiffness calibration. (b) Longitudinal stiffness calibration curves under different loadings. (c) Vertical deflection test result for the calibration of the vertical stiffness,  $k_t$ .

**TABLE I**  
CALIBRATION RESULTS OF THE LONGITUDINAL STIFFNESS

loading (N)	50	81	123
$k_\xi$ (N/mm)	69.5	113.0	198.1

**TABLE II**  
PARAMETERS RELATED TO THE TIRE MODEL

$E$ (MPa)	$\nu$	$E^*$ (MPa)	$k_t$ (N/mm)	$R_b$ (m)	$h_t$ (m)
3.88	0.35	4.42	38.92	0.12	0.007

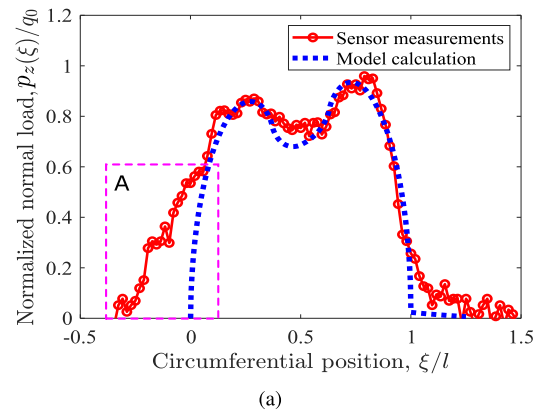
The external friction force  $f_f$  is regarded as a spring-like force

$$f_f = k_\xi \delta(h_t) = \frac{k_\xi h_t^3}{3EI} f_s(h_t) \quad (18)$$

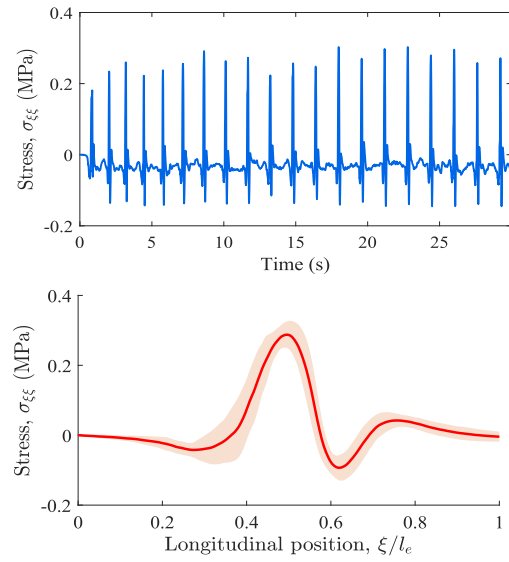
and (17) is used. By calculating the coefficient in (18), we obtain the estimate of the longitudinal stiffness  $k_\xi$ .

To conduct the calibration process, a static pulling test was conducted, and a small supporting fixture was designed, as shown in Fig. 7(a). The tire was loaded and supported on the small fixture, so that the local deformation was created by pulling the cable connected with the rim of the wheel. The pulling force was increased gradually and measured by the load cell. During the pulling process, the tire did not slip or rotate. By computing the slope of the linear fitting curve, we obtained the estimate of  $k_\xi$ . Fig. 7(b) shows the plots at different normal loads, and Table I lists the corresponding calibration results. As the normal load increased, the calibrated stiffness increased accordingly. We interpolated and extrapolated linearly for longitudinal stiffness values at various normal loading conditions.

To obtain the tire vertical stiffness  $k_t$ , deflection tests were conducted. The tire was loaded steadily to several target normal load readings by lifting the jack up. A cable-type potentiometer simultaneously measured the deflection of the tire with the recorded normal loads. Fig. 7(c) shows the calibration test measurements for stiffness  $k_t$  (i.e., the slope of the fitted line) under inflation pressure  $P_{air} = 158$  kPa. Table II lists the estimated values of a set of the model parameters, including  $k_t$ . By (16), coefficient  $K$  is calculated as  $K = 64k_t/(81h_t\pi^4) = 4.52 \times 10^4$ . In this work, all rubber-related model parameters are assumed constant.



(a)



(b)

**Fig. 8.** (a) Normalized contact pressure distribution comparison results. (b) Consistency of the sensor measurements.

## B. Results

The contact pressure distribution by (3) was validated through comparing with measurements from the embedded sensors. Fig. 8(a) shows the normal load distribution under traction on the contact patch with  $P_{air} = 158$  kPa. The magnitude was normalized by the average pressure  $p_0 = (F_z/l)$ . For the main portion of the contact patch, the model

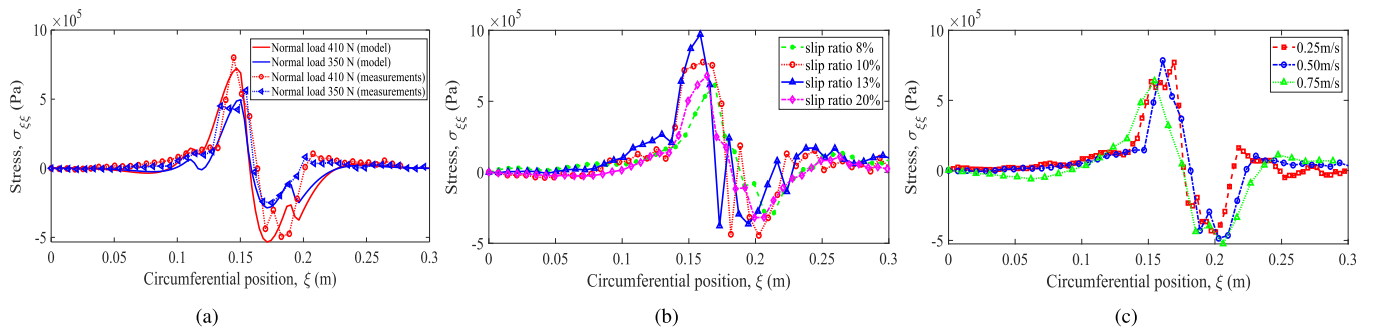


**Fig. 9.** Internal stress by the sensor measurements under various working conditions. (a) Two different normal loads, with  $v_x = 0.5$  m/s and  $s = 10\%$ . (b) Various slip ratio conditions, with  $v_x = 1$  m/s and  $F_z = 410$  N. (c) Varied linear velocities, with  $s = 10\%$  and  $F_z = 410$  N.

prediction matches the sensor measurements closely. The predicted first hump near the leading edge by the model was lower than that near the trailing edge. It is primarily because the bending effect and low inflation pressure together brought the large deformation and stress concentration at two shoulders of the contact patch. Furthermore, there is a clear discrepancy in region A in Fig. 8(a), and this is due to the precontact tire rubber bending effect. The consistency of the sensor measurements was tested to check the repeatability and reliability. During the test, tire rotation velocity, tire normal load, and relative slip were maintained the same. The top plot in Fig. 8(b) shows the sensing signal profile. For each cycle, the embedded sensor entered the contact patch and generated corresponding signal for the internal stress. The bottom plot in Fig. 8(b) confirms the mean and variation of the sensing signal in a normalized, longitudinal direction. The variation of the measurements was consistent and not significant.

A set of tests was conducted for analyzing how the sensor responded when the normal load, slip ratio, and velocity changed. In each set of tests, only one working condition varied, while others were maintained the same. Due to the limited motor power and driving torque, the maximum linear velocity of the wheel was 1.25 m/s, and the maximum tire load was 550 N. In all tests, the velocity and normal load did not exceed these limits. Fig. 9(a) shows the stress  $\sigma_{\xi\xi}$  by the sensor measurements and the model predictions under various normal loads. The corresponding velocity and surface slip ratio were maintained as  $v_x = 0.5$  m/s and  $s = 10\%$ . It is shown that the both amplitudes of two peaks of the stress curve (tensile and compressed state) became large, as the normal load increased from 350 to 410 N. The sensor measurements show a consistent trend. Various slip conditions were recreated through slowing down the belt speed. Meanwhile, the normal load was kept at  $F_z = 410$  N, and the wheel rotation was maintained constantly for  $v_x = 1$  m/s. Fig. 9(b) shows the tire internal stress under various slip ratios. A large slip ratio did not result in a high magnitude of the longitudinal internal stress. As demonstrated, the positive magnitude of tensile stress started to grow with the increasing slip (from  $s = 8\%-13\%$ ) toward the leading edge of the contact patch. However, the positive peak value became small when the slip kept growing beyond a certain value (from  $s = 13\%-20\%$ ). It is well known that the resultant friction force depends on slip ratio. In small slip region, the friction force grows, as slip

ratio increases, and it decreases in the large slip region. The sensor measurements reflected and confirmed this trend.

The velocity also influences the internal stress on the contact patch. Fig. 9(c) shows the stress results from sensor measurements with different velocities at  $s = 10\%$  and  $F_z = 410$  N. There was a slight difference among three velocity conditions, namely,  $v_x = 0.25$ , 0.5, and 0.75 m/s. The positive maximum value decreased when the velocity became large, and the location moved toward the leading edge. The velocity does not play a dominant role for the external friction force and internal stress in the small slip region, such as  $s \leq 10\%$ . The above results confirm that the force-sensitive sensor is able to capture the internal stress when working conditions change.

To demonstrate the friction estimation, we conducted experiments that involved real-time instantaneous friction prediction on different surfaces. Three types of road surface conditions were created and simulated: regular, rough, and smooth surfaces. Two treadmill belts were prepared for creating these surface conditions. Asphalt painting was coated on one belt to increase roughness of the contact surface to create high-friction condition, while smooth and strongly adhesive tape was attached to the tire to create a smooth contact situation for tests on low-friction surface.

Fig. 10(a) and (d) shows the friction estimation results on the regular surface. The wheel rotation speed and the tire normal load were both controlled and maintained at  $v_x = 1.0$  m/s and  $F_z = 245$  N. As shown in Fig. 10(a), relative slip was controlled and fluctuated between  $s = 0\%$  and 80% through slowing down and fastening the belt translation speed. Fig. 10(d) shows the corresponding friction force estimation results. The blue curve was from friction index that was calculated from the embedded sensor measurements, while the red one was direct load cell recordings. As the slip ratio changed, the resultant friction force also changed simultaneously. The embedded sensor prediction showed the similar temporal profile of the friction force despite that there were some differences in terms of magnitudes of signal peaks. The discrepancies might come from signal noise of the embedded sensor as well as possibly inconsistent contact of the sensor film and the rubber layer. The same experimental processes were conducted on the rough and smooth surfaces. Fig. 10(b) and (e) [Fig. 10(c) and (f)] shows the results on the rough (smooth) surface. Different from results on the regular and rough surface tests, large initial tire slip was observed

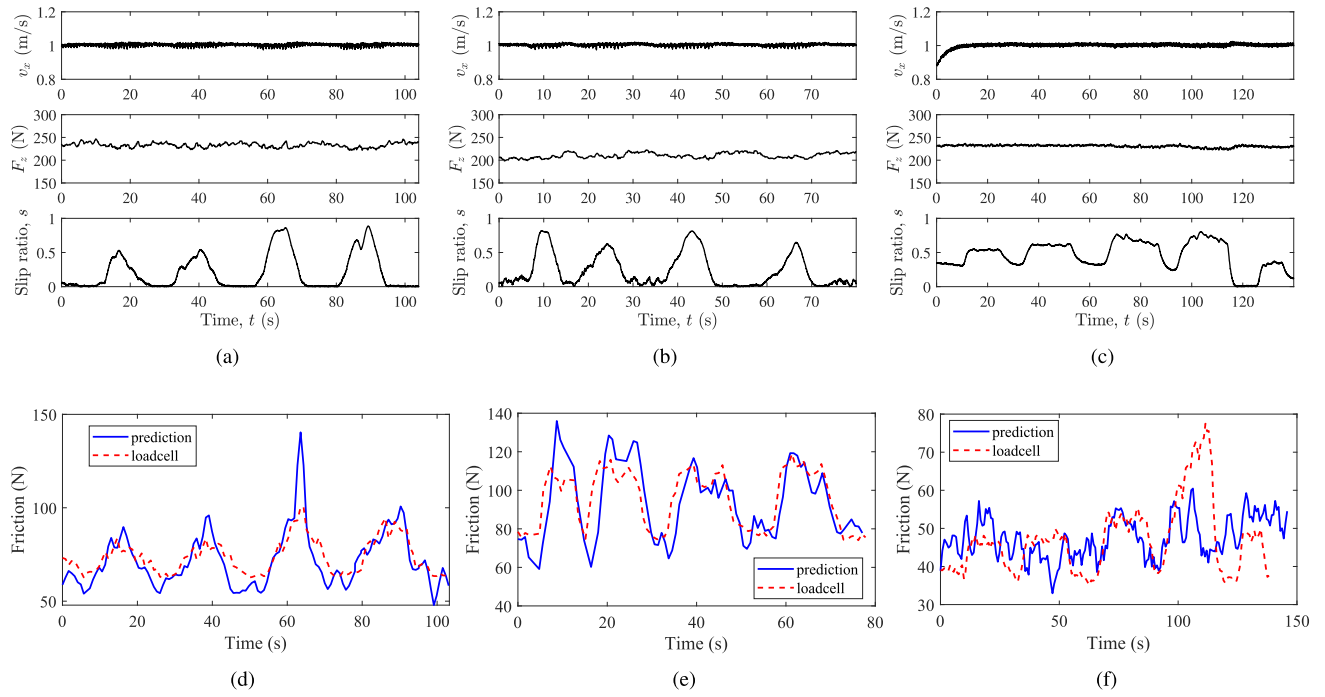


**Fig. 10.** Friction estimation results on three different surfaces. (a)–(c) Working conditions of the rotation velocity, tire normal load, and relative slip ratio pattern on the regular, rough, and smooth surfaces, respectively. (d)–(f) Comparison between friction force estimation from the flexible sensor measurements and load cell on the regular, rough, and smooth surfaces, respectively.

**TABLE III**  
PARAMETERS IDENTIFIED IN THE LUGRE MODEL  
UNDER THREE ROAD SURFACES

Surface condition	$\mu_s$	$\mu_c$	$v_s$
Regular	0.341	0.10	2.17
Rough	0.524	0.11	1.43
Smooth	0.238	0.11	3.34

around  $s = 50\%$  on the smooth surface. Furthermore, the friction force prediction by sensor measurements showed some oscillations, which deteriorated the estimation performance.

The tire friction–slip curve was also predicted by using embedded sensor measurements. The steady-state LuGre friction model was used to calculate friction and relate the friction index. A set of model parameters representing friction–slip characteristics were selected, including static and Coulomb friction coefficients  $\mu_s$  and  $\mu_c$  as well as Stribeck velocity  $v_s$  in function  $g(v_r)$  in (6). A nonlinear optimization problem was formulated to estimate these model parameters, that is,

$$(\mu_s^*, \mu_c^*, v_s^*) = \underset{\mu_s, \mu_c, v_s}{\operatorname{argmin}} \sum_s |F_f^{\text{LuG}}(s) - F_f(s)|^2$$

where  $F_f(s)$  is the friction estimation by (16). The analytical solution of the LuGre friction model was obtained as follows [33]:

$$F_f^{\text{LuG}} = F_z g(v_r) \left[ 1 + \frac{6x_c}{x_a} (x_c - 1) \right] + \sigma_2 v_r l \quad (19)$$

where  $x_c$  is the boundary location of the adhesion and sliding regions of the contact patch. Details of this analytical boundary location can be found in [33, Appendix].

**Table III** lists the identified model parameters for three surface conditions. Using these parameter values, Fig. 11 shows the identification results of friction–slip curves on three surface conditions. Using the embedded sensor measurements provided an accurate friction–slip curve in a wide slip range, especially on regular and rough surfaces; see Fig. 11(a) and (b). It is interesting to find that in the large slip region, the friction coefficient calculated by sensor estimations increased slightly rather than reducing on the regular and rough surfaces shown in Fig. 11(a) and (b). Compared with commonly reported friction–slip curves, this difference might be due to the belt deformation and elongation, and the viscous effect under large slip condition. The estimation performance confirms that the sensor measurements provide accurate friction characteristics in the slip region of interest, e.g., from  $s = 0\%$  to  $60\%$ .

Only one sensor was embedded inside the tire at the center of the cross section, as shown in Fig. 1(b). We only used one sensor primarily because of limited embedding space of the small-size tire/ground contact patch of the tire tread. Furthermore, we attempted to minimize the destructive effect of the cutting tread rubber on the tread stress. Each sensor has four independent sensing cells, which can measure forces at different locations inside the tread. As already demonstrated, one embedded sensor can provide sufficient signals to extract the tire/road contact information. For the comparison purpose, we also embedded two sensors at different circumferential locations and collected sensor recordings under the same controlled working conditions. In addition, we further conducted the experiments to embed sensors into another large-size aircraft tire. Although, due to page limit, we did not present these results, they confirmed the

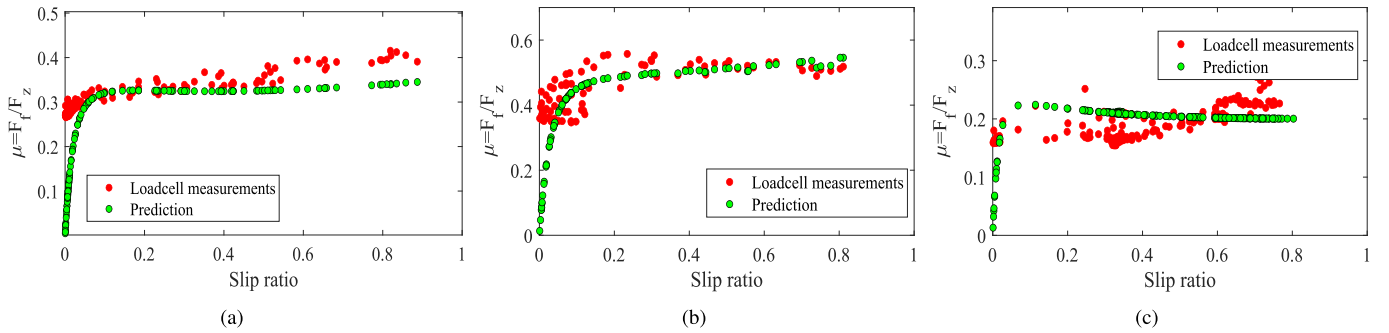


**Fig. 11.** Friction coefficient–slip curves on different surfaces. Green dots are predictions from the steady-state LuGre model, and red dots are directly from friction load cells. (a) Regular belt surface. (b) Rough belt surface. (c) Smooth belt surface.

consistent signal patterns and trends of the embedded sensor outcomes.

Although the experimental results demonstrated feasibility of the flexible sensors for friction force prediction and characteristics, there are still some limitations in this work. First, this work did not investigate the influence of the tire lateral force on the sensor interpretation model and force estimation. Second, the testing tire velocity and normal load were not high enough compared with real vehicle applications. This was mainly due to the limited power and speed of the driving motor of the test bed. Third, the internal contact condition between the rubber and sensing film certainly influenced the signal pattern. It was challenging to guarantee reliable well-contacted conditions during all tests. Finally, the surface condition of the treadmill belt might not completely represent the real road surfaces (e.g., asphalt and concrete surfaces). A new test platform and experimental protocols are under design to further extend and demonstrate the friction estimation application.

## VI. CONCLUSION

In this article, a force-sensitive-based sensor was selected and embedded inside the tire rubber layer to investigate the dynamic tire/road interaction estimation for real-time applications. To interpret sensor measurements, an integrated tread beam and the LuGre friction model were built to compute rubber deformation and internal stress distribution on the contact patch. A sensor interpretation model was developed, and sensing curves were analyzed to obtain the external friction force estimation. The sensitivity of the sensor measurements was tested, and tire/road friction estimations were conducted for different surface conditions. Experimental results showed the feasibility of the force sensor for predicting dynamic tire/road friction forces and friction coefficient–slip characteristics. One ongoing research plan includes to use the proposed intelligent tire system for field testing. Comparison with other friction measurement equipment will be also conducted to help evaluate friction coefficient under various road conditions.

## APPENDIX

For small slip,  $s \ll 1$ , it is assumed that there is no significant deformation by translation motion, that is,  $u(\xi) \approx 0$  and  $\phi(\xi) \approx 0$  for  $\xi \in [0, l_e]$ . Given this condition, the internal stress and sensor measurements include two parts that  $-w(\xi)$  and  $d^2w(\xi)/d\xi^2$ .

From (1), we calculate the first derivative with respect to  $\xi$

$$w'(\xi) = \frac{M_a}{2\beta_1\beta_2 EI} \begin{cases} e^{-\beta_1(a-\xi)}[\beta_2 \cos \gamma - \beta_1 \sin \gamma], & \xi \leq a \\ e^{-\beta_1(\xi-a)}[\beta_2 \cos \gamma + \beta_1 \sin \gamma], & \xi > a \end{cases}$$

where  $\gamma = \beta_2(a - \xi)$ . Denoting  $\alpha = \tan^{-1}(\beta_1/\beta_2)$ , we obtain

$$w'(\xi) = \frac{M_a \sqrt{\beta_1^2 + \beta_2^2}}{2\beta_1\beta_2 EI} \begin{cases} e^{-\frac{\beta_1}{\beta_2}\gamma} \cos(\alpha + \gamma), & \gamma \geq 0 \\ e^{\frac{\beta_1}{\beta_2}\gamma} \cos(\alpha - \gamma), & \gamma < 0. \end{cases}$$

Similarly, we take the second derivative of  $w(\xi)$  and obtain

$$w''(\xi) = \frac{M_a(\beta_1^2 + \beta_2^2)}{2\beta_1\beta_2 EI} \begin{cases} e^{-\frac{\beta_1}{\beta_2}\gamma} \sin(2\alpha + \gamma), & \gamma \geq 0 \\ -e^{\frac{\beta_1}{\beta_2}\gamma} \sin(2\alpha - \gamma), & \gamma < 0. \end{cases}$$

Therefore,  $w''(\xi)$  can be rewritten as follows:

$$w''(\xi) = \frac{(\beta_1^2 + \beta_2^2)}{2\beta_1\beta_2 EI} e^{-\frac{\beta_1}{\beta_2}|\gamma|} \sin(2\alpha + |\gamma|) M_a.$$

Recall (2) that  $\beta_1 \approx \beta_2$  when the internal longitudinal force  $T_\xi$  is small compared with  $4\sqrt{EIk_t}$ , we rewrite  $w(\xi)$  and  $w''(\xi)$  as follows:

$$w(\xi) = \frac{M_a}{\sqrt{k_t EI}} e^{-|\gamma|} \sin(-\gamma), \quad w''(\xi) = \frac{M_a}{EI} e^{-|\gamma|} \cos(|\gamma|) M_a$$

with  $2\alpha = \pi/2$ . For tire rubber properties, the coefficients  $1/\sqrt{k_t EI} \ll 1/EI$ , and then,  $w(\xi) \ll w''(\xi)$ . Hence, the sensor measurement is mainly proportional to  $w''(\xi)$ .

When  $\gamma = 0$ ,  $w''(\xi)$  achieves the maximum value and  $w(\xi) = 0$ , while  $w''(\xi)$  is at the minimum value when  $\gamma = \gamma_c$ , where  $\gamma_c$  satisfies

$$w^{(3)}(\xi)|_{\gamma_c} = -(\cos \gamma_c + \sin \gamma_c) e^{-\gamma_c} = 0, \quad \gamma_c > 0.$$

Checking the solution  $\gamma_c \in [0, \pi]$ , we obtain  $\gamma_c = 3\pi/4$ . Therefore, two feature points  $\gamma = 0$  and  $\gamma = \gamma_c = 3\pi/4$  are selected to capture the curve characteristics of  $w''(\xi)$ . From the discussion in Section IV,  $\gamma = 0$  is applied for points  $P_{s1}$ ,  $I_1$ , and  $I_2$ , while  $\gamma = \gamma_c$  is applied for point  $P_{s2}$ . The maximum value of  $w''(\xi)$  is

$$A_{w1} = \frac{(\beta_1^2 + \beta_2^2)}{2\beta_1\beta_2 EI} M_a = \frac{M_a}{EI}$$

when  $\sin(2\alpha + |\gamma|) = 1$ . From above calculation, the peak-to-peak spacial distance is  $\Delta\xi = \gamma_c/\beta_2$ .

## REFERENCES

- [1] H. Lee and S. Taheri, "Intelligent tires? A review of tire characterization literature," *IEEE Intell. Transp. Syst. Mag.*, vol. 9, no. 2, pp. 114–135, Summer 2017.
- [2] S. Yang, Y. Chen, R. Shi, R. Wang, Y. Cao, and J. Lu, "A survey of intelligent tires for tire-road interaction recognition," *IEEE Trans. Intell. Veh.*, vol. 7, no. 3, pp. 520–532, Sep. 2022.
- [3] F. Braghin, M. Brusarosco, F. Cheli, A. Cigada, S. Manzoni, and F. Mancuso, "Measurement of contact forces and patch features by means of accelerometers fixed inside the tire to improve future car active control," *Vehicle Syst. Dyn.*, vol. 44, no. 1, pp. 3–13, Jan. 2006.
- [4] A. Niskanen and A. Tuononen, "Three three-axis piez accelerometers on the inner liner of a tire for finding the tire-road friction potential indicators," *Sensors*, vol. 15, no. 8, pp. 19251–19263, 2015.
- [5] Z. Zou, X. Zhang, Y. Zou, and B. Lenzo, "Tire-road friction coefficient estimation method design for intelligent tires equipped with three-axis accelerometer," *SAE Int. J. Vehicle Dyn., Stability, NVH*, vol. 5, no. 3, pp. 249–258, May 2021.
- [6] N. Xu, H. Askari, Y. Huang, J. Zhou, and A. Khajepour, "Tire force estimation in intelligent tires using machine learning," *IEEE Trans. Intell. Transp. Syst.*, vol. 23, no. 4, pp. 3565–3574, Apr. 2022.
- [7] H.-J. Kim et al., "A road condition classification algorithm for a tire acceleration sensor using an artificial neural network," *Electronics*, vol. 9, no. 3, p. 404, Feb. 2020.
- [8] D. Lee, J.-C. Kim, M. Kim, and H. Lee, "Intelligent tire sensor-based real-time road surface classification using an artificial neural network," *Sensors*, vol. 21, no. 9, p. 3233, May 2021.
- [9] R. G. Longoria, R. Brushaber, and A. Simms, "An in-wheel sensor for monitoring tire-terrain interaction: Development and laboratory testing," *J. Terramechanics*, vol. 82, pp. 43–52, Apr. 2019.
- [10] R. Matsuzaki, T. Keating, A. Todoroki, and N. Hiraoka, "Rubber-based strain sensor fabricated using photolithography for intelligent tires," *Sens. Actuators A, Phys.*, vol. 148, no. 1, pp. 1–9, Nov. 2008.
- [11] W. Zhao, C. Zhang, and J. Zhang, "Continuous measurement of tire deformation using long-gauge strain sensors," *Mech. Syst. Signal Process.*, vol. 142, Aug. 2020, Art. no. 106782.
- [12] D. Garcia-Pozuelo, O. Olatunbosun, J. Yunta, X. Yang, and V. Diaz, "A novel strain-based method to estimate tire conditions using fuzzy logic for intelligent tires," *Sensors*, vol. 17, no. 2, pp. 350–365, 2017.
- [13] M. F. Mendoza-Petit, D. García-Pozuelo, V. Díaz, and O. Olatunbosun, "A strain-based intelligent tire to detect contact patch features for complex maneuvers," *Sensors*, vol. 20, no. 6, p. 1750, Mar. 2020.
- [14] M. F. Mendoza-Petit, D. García-Pozuelo, V. Díaz, R. Gutiérrez-Moizant, and O. Olatunbosun, "Automatic full slip detection system implemented on the strain-based intelligent tire at severe maneuvers," *Mech. Syst. Signal Process.*, vol. 183, Jan. 2023, Art. no. 109577.
- [15] E. G. Armstrong, C. Sandu, and S. Taheri, "Investigation into use of piezoelectric sensors in a wheeled robot tire for surface characterization," *J. Terramechanics*, vol. 62, pp. 75–90, Dec. 2015.
- [16] G. Erdogan, L. Alexander, and R. Rajamani, "Estimation of tire-road friction coefficient using a novel wireless piezoelectric tire sensor," *IEEE Sensors J.*, vol. 11, no. 2, pp. 267–279, Feb. 2011.
- [17] J. Yi, "A piezo-sensor-based 'smart tire' system for mobile robots and vehicles," *IEEE/ASME Trans. Mechatronics*, vol. 13, no. 1, pp. 95–103, Feb. 2008.
- [18] Z. Quan, B. Li, S. Bei, X. Sun, N. Xu, and T. Gu, "Tire-road friction coefficient estimation method design for intelligent tires equipped with PVDF piezoelectric film sensors," *Sens. Actuators A, Phys.*, vol. 349, Jan. 2023, Art. no. 114007.
- [19] Y. Zhang, A. W. Allen, J. Yi, and T. Liu, "Understanding tire-road stick-slip interactions with embedded rubber force sensors," in *Proc. IEEE/ASME Int. Conf. Adv. Intell. Mechatronics (AIM)*, Kaohsiung, Taiwan, Jul. 2012, pp. 550–555.
- [20] Y. Zhang, J. Yi, and T. Liu, "Embedded flexible force sensor for in-situ tire-road interaction measurements," *IEEE Sensors J.*, vol. 13, no. 5, pp. 1756–1765, May 2013.
- [21] Y. Zhang and J. Yi, "Static tire/road stick-slip interactions: Analysis and experiments," *IEEE/ASME Trans. Mechatronics*, vol. 19, no. 6, pp. 1940–1950, Dec. 2014.
- [22] M. S. Pegram, T. R. Botha, and P. S. Els, "Full-field and point strain measurement via the inner surface of a rolling large lug tire," *J. Terramechanics*, vol. 96, pp. 11–22, Aug. 2021.
- [23] D. Garcia-Pozuelo, O. Olatunbosun, S. Strano, and M. Terzo, "A real-time physical model for strain-based intelligent tires," *Sens. Actuators A, Phys.*, vol. 288, pp. 1–9, Apr. 2019.
- [24] H. Lee and S. Taheri, "A novel approach to tire parameter identification," *Proc. Inst. Mech. Eng., D, J. Automobile Eng.*, vol. 233, no. 1, pp. 55–72, Jan. 2019.
- [25] H. Zhou et al., "A strain-based method to estimate longitudinal force for intelligent tires by using a physics-based model," *Strojníški vestnik-J. Mech. Eng.*, vol. 67, no. 4, pp. 153–166, Apr. 2021.
- [26] N. Xu, E. Hashemi, Z. Tang, and A. Khajepour, "Data-driven tire capacity estimation with experimental verification," *IEEE Trans. Intell. Transp. Syst.*, vol. 23, no. 11, pp. 21569–21581, Nov. 2022.
- [27] J. B. Andrews, J. A. Cardenas, C. J. Lim, S. G. Noyce, J. Mullett, and A. D. Franklin, "Fully printed and flexible carbon nanotube transistors for pressure sensing in automobile tires," *IEEE Sensors J.*, vol. 18, no. 19, pp. 7875–7880, Oct. 2018.
- [28] H. Xiang, M. Trkov, K. Yu, and J. Yi, "A stick-slip interactions model of soft-solid frictional contacts," *J. Dyn. Syst., Meas., Control*, vol. 141, no. 4, Apr. 2019, Art. no. 041015.
- [29] Y. Gong, X. Chen, J. Yi, and H. Wang, "Hydrodynamics and friction estimation for wet tire/ground interactions," in *Proc. Amer. Control Conf. (ACC)*, San Diego, CA, USA, May 2023, pp. 3175–3180.
- [30] J. Pauwelussen, *Essentials of Vehicle Dynamics*. Oxford, U.K.: Butterworth-Heinemann, 2014.
- [31] R. Solecki and R. J. Conant, *Advanced Mechanics of Materials*. London, U.K.: Oxford Univ. Press, 2003.
- [32] V. L. Popov, M. Heß, and E. Willert, *Handbook of Contact Mechanics: Exact Solutions of Axisymmetric Contact Problems*. Berlin, Germany: Springer, 2019.
- [33] J. Li, Y. Zhang, and J. Yi, "A hybrid physical-dynamic tire/road friction model," *J. Dyn. Syst., Meas., Control*, vol. 135, no. 1, Jan. 2013, Art. no. 011007.
- [34] X. Chen, J. Yi, J. Qian, and H. Wang, "An integrated tread beam/LuGre tire-road friction model," *IFAC-PapersOnLine*, vol. 55, no. 37, pp. 688–693, 2022.
- [35] R. Schmidt, *Advances in Aircraft Brakes and Tires*. Warrendale, PA, USA: SAE International, 2015, pp. 29–37.



**Xunjie Chen** received the B.S. degree in vehicle engineering from Jilin University, Changchun, China, in 2018, and the M.Eng. degree in vehicle engineering from Tongji University, Shanghai, China, in 2021. He is currently pursuing the Ph.D. degree in mechanical and aerospace engineering with Rutgers University, Piscataway, NJ, USA.

His research interests include dynamic systems and control, tire dynamics modeling, and interaction force modeling for robotic systems.



**Rishikesh Sathyanarayan** received the B.S. degree in mechanical and aerospace engineering from Rutgers University, Piscataway, NJ, USA, in 2023. He is currently pursuing the Ph.D. degree with the Department of Mechanical Engineering and Material Science, Yale University, New Haven, CT, USA.

His work as an undergraduate focused on experimental studies on aircraft tire-runway interactions, and mechanical design and control of underactuated robots. His current research interests include active learning and sensing, control systems, and mechatronics, with applications to robot locomotion and exploration.

Mr. Sathyanarayan was a recipient of the 2023 Robert E. Apfel Fellowship upon joining Yale.



**Yongbin Gong** received the B.S. degree in thermal engineering from the Huazhong University of Science and Technology, Wuhan, China, in 2011, and the M.Eng. degree in mechanical engineering from Rutgers University, Piscataway, NJ, USA, in 2018, where he is currently pursuing the Ph.D. degree in mechanical and aerospace engineering.

His research interests include dynamic systems and control, and tire dynamics modeling.



**Jingang Yi** (Senior Member, IEEE) received the B.S. degree in electrical engineering from Zhejiang University, Hangzhou, China, in 1993, the M.Eng. degree in precision instruments from Tsinghua University, Beijing, China, in 1996, and the M.A. degree in mathematics and the Ph.D. degree in mechanical engineering from the University of California at Berkeley, Berkeley, CA, USA, in 2001 and 2002, respectively.

He is currently a Professor of Mechanical Engineering with Rutgers University, Piscataway, NJ, USA. His research interests include autonomous robotic systems, dynamic systems and control, mechatronics, and automation science and engineering, with applications to biomedical systems, civil infrastructure, and transportation systems.

Dr. Yi is a Fellow of the American Society of Mechanical Engineers (ASME). He was a recipient of the 2010 U.S. NSF CAREER Award. He served as a Senior Editor for the IEEE ROBOTICS AND AUTOMATION LETTERS and an Associate Editor for the IEEE TRANSACTIONS ON AUTOMATION SCIENCE AND ENGINEERING, the IEEE/ASME TRANSACTIONS ON MECHATRONICS, the IEEE ROBOTICS AND AUTOMATION LETTERS, *IFAC Journal Mechatronics, Control Engineering Practice*, and the *ASME Journal of Dynamic Systems, Measurement and Control*. He serves as a Senior Editor for the IEEE TRANSACTIONS ON AUTOMATION SCIENCE AND ENGINEERING and an Associate Editor for the *International Journal of Intelligent Robotics and Applications*.



**Hao Wang** received the Ph.D. degree in civil engineering from the University of Illinois at Urbana–Champaign, Urbana, IL, USA, in 2011.

He is currently a Professor and the Graduate Director of Civil and Environmental Engineering with Rutgers University, Piscataway, NJ, USA. His research interests include sustainable and smart infrastructure materials and transportation systems.